Astronomy & Astrophysics manuscript no. kepler˙full˙arxiv
July 29, 2015
© ESO 2015

arXiv:1507.07757v1 [astro-ph.SR] 28 Jul 2015

Rotation, differential rotation, and gyrochronology of active Kepler stars

Timo Reinhold[1], Laurent Gizon[1,2]

[1] Institut für Astrophysik, Georg-August-Universität Göttingen, 37077 Göttingen, Germany
[2] Max-Planck-Institut für Sonnensystemforschung, Justus-von-Liebig-Weg 3, 37077 Göttingen, Germany

Received day month year / Accepted day month year

Abstract

Context. Apart from the discovery of hundreds of exoplanets, the high-precision photometry from the CoRoT and Kepler satellites has led to measurements of surface rotation periods for tens of thousands of stars, which can potentially be used to infer stellar ages via gyrochronology.
Aims. Our main goal is to derive ages of thousands of field stars using consistent rotation period measurements derived by different methods. Multiple rotation periods are interpreted as surface differential rotation (DR). We study the dependence of DR with rotation period and effective temperature.
Methods. We re-analyze the sample of 24,124 Kepler stars from Reinhold et al. (2013) using different approaches based on the Lomb-Scargle periodogram. Each quarter (Q1–Q14) is treated individually using a prewhitening approach. Additionally, the full time series, and different segments thereof are analyzed.
Results. For more than 18,500 stars our results are consistent with the rotation periods from McQuillan et al. (2014). Thereof, more than 12,300 stars show multiple significant peaks, which we interpret as DR. Dependencies of the DR with rotation period and effective temperature, as shown in Reinhold et al. (2013), could be confirmed, e.g. the relative DR increases with rotation period. Gyrochronology ages between 100 Myr and 10 Gyr were derived for more than 17,000 stars using different gyrochronology relations, most of them with uncertainties dominated by period variations. We find a bimodal age distribution for $T_{\rm eff}$ between 3200–4700 K. The derived ages reveal an empirical activity-age relation using photometric variability as stellar activity proxy. Additionally, we found 1079 stars with extremely stable (mostly short) periods. Half of these periods may be associated with rotation stabilized by non-eclipsing companions, the other half might be due to pulsations.
Conclusions. The derived gyrochronology ages are well constrained since more than $\sim 93.0\,\%$ of the stars seem to be younger than the Sun where calibration is most reliable. Explaining the bimodality in the age distribution is challenging, and limits accurate stellar age predictions. The relation between activity and age is interesting, and requires further investigation. The existence of cool stars with almost constant rotation period over more than three years of observation might be explained by synchronization with stellar companions, or a dynamo mechanism keeping the spot configurations extremely stable.

Key words. stars: starspots – stars: rotation

1. Introduction

Encouraged by high-precision photometry of the CoRoT and Kepler satellites, measurements of stellar rotation periods have become numerous in recent years, unprecedented in their number and accuracy (Meibom et al. 2011a; Affer et al. 2012; McQuillan et al. 2013a; Nielsen et al. 2013; McQuillan et al. 2013b; Walkowicz & Basri 2013; Reinhold et al. 2013; McQuillan et al. 2014). Owing to magnetic braking, the rotation period of a star is linked to its age. Stellar winds carry away charged particles along the magnetic field lines. As time proceeds, more and more material is dissipated, making the star slower and slower. This angular momentum loss over the stars' lifetime results in the fact that young stars rotate faster than old ones, on average.

A relation between stellar age and rotation period was first shown by Skumanich (1972). This author further demonstrated that the level of chromospheric activity depends on the stellar age. Succeeding measurements at the Mount Wilson Observatory corroborated the relations between chromospheric activity index $R'_{\rm HK}$, the rotation period, and the stellar age (Noyes et al. 1984; Soderblom et al. 1991). Additionally, since the 1980s fast rotators are known to exhibit enhanced X-ray activity (Pallavicini et al. 1981; Pizzolato et al. 2003). These coherencies are now established as activity-rotation-age relation.

The stellar age cannot be measured directly but has to be inferred from other quantities. In principle, activity-age relations can be used to infer stellar ages, although their accuracy suffers from secular changes of the activity level. A classical method to infer stellar ages is isochrone modeling. The ages of stellar clusters can be inferred from this method (see, e.g., Perryman et al. 1998), provided some knowledge of effective temperature, luminosity, and metallicity. This method can also be applied to field stars, however with typical uncertainties on the order of 20–30 %.

Over the past years, *gyrochronology* has become a promising method to derive stellar ages from their rotation

Send offprint requests to: T. Reinhold,
e-mail: reinhold@astro.physik.uni-goettingen.de

periods (Barnes 2003, 2007; Mamajek & Hillenbrand 2008; Meibom et al. 2009; Collier Cameron et al. 2009; James et al. 2010; Barnes 2010; Delorme et al. 2011; Meibom et al. 2011b). Barnes (2003, 2007) collected rotation periods from open clusters of different ages, and identified two sequences in the color-period diagram, namely the I- and C-sequence. Using known cluster ages, this author derived empirical fits to the color (mass) dependence of the data on the I-sequence, according to

$$P_I(B-V,t) = f(B-V)\, g(t). \quad (1)$$

The function $g(t) \propto t^{1/2}$ is the rotation-age relation from Skumanich (1972), and $f(B-V)$ an empirical fit to the $(B-V)_0$ color dependence of the rotation period P_I of the I-sequence stars reflecting their braking efficiency. $(B-V)_0$ colors are used as a substitute for stellar mass instead. Unfortunately, gyrochronology is poorly calibrated for old stars. Meibom et al. (2011a) measured rotation periods for the 1 Gyr old cluster NGC 6811 in the Kepler field. The oldest star used for calibration was the Sun with an age of 4.55 Gyr. Bridging this large gap Meibom et al. (2015) recently measured rotation periods of 30 stars in the 2.5 Gyr old cluster NGC 6819, deriving a well-defined period-age-mass relation. At later ages wide binaries might help constraining the age-rotation relation (Chanamé & Ramírez 2012).

Another method to determine stellar ages is provided by asteroseismology (see, e.g., Chaplin et al. 2014). Recently, efforts are underway to calibrate asteroseismology ages by comparing them to gyrochronology measurements (García et al. 2014; do Nascimento et al. 2014; Lebreton & Goupil 2014; Angus et al. 2015). Furthermore, Vidotto et al. (2014) found a correlation between the average large-scale magnetic field strength and the stellar age according to $\langle |B_V| \rangle \propto t^{-0.655}$ similar to Skumanich's law, calling this method *magnetochronology*. A review article on various age dating methods was provided by Soderblom (2010).

Gyrochronology relies on age calibration using open clusters of different ages, assuming their stars to be coeval. Calibration becomes difficult for clusters older than $\sim$1 Gyr, though. One reason is that rotation periods are difficult to measure for slowly rotating stars. Furthermore, clusters become disrupted at that age (the degree strongly depends on the initial stellar cluster density), rendering the cluster membership of individual stars uncertain. Additionally, gyrochronology relations are calibrated only for main sequence dwarfs. Bulk rotation period measurements might be largely contaminated by subgiants (van Saders & Pinsonneault 2013), which have started evolving off the main sequence. Thus, applying gyrochronology relations using subgiant rotation periods might lead to a mis-classification of their evolutionary state (Doğan et al. 2013).

Further uncertainties result from the fact that a star is by no means a rigid rotator with a well-defined rotation period. High-precision instruments like the CoRoT and Kepler telescopes provide the opportunity to observe multiple rotation periods associated with latitudinal differential rotation, which was observed for many active stars (Reinhold et al. 2013). Moreover, spot rotation periods heavily rely on their evolutionary timescales, which becomes more important for less active stars. Both effects may contribute large uncertainties to the rotation period used in the color-period fits.

Despite these drawbacks, gyrochronology relations supply a straightforward way to infer stellar ages of field stars. Other approaches to measure stellar ages are usually accompanied with large errors. Isochrone methods collapse for binary stars, which are assumed to be coeval, but do not appear on the same isochrone if the companions exhibit different masses. Asteroseismology ages strongly depend on some (usually unknown) model parameters (e.g., metallicity), which can lead to large errors.

The knowledge of stellar ages is of utmost interest for galactic formation. We aim to provide stellar ages for thousands of stars, inferred from mean rotation period measurements via gyrochronology. Furthermore, we show that multiple significant periods are quite common among active stars, which we assign to surface differential rotation. These period fluctuations dominate the age uncertainties. As opposed to this, we also found a sub-sample of stars almost showing no period variations over more than three years of observation.

The paper is organized as follows: Sect. 2 presents the Kepler data products. The different approaches used to analyze the data are explained in Sect. 3. Sect. 4 contains the results, which are further discussed in Sect. 5. We close with a brief summary of our results in Sect. 6.

2. Kepler data

The Kepler satellite provides almost continuous observations of the same field for more than four years (May 2, 2009 - May 11, 2013). The data is delivered in quarters (Q0–Q17), each of $\sim$90 d length (Q2–Q16), with exceptions for the commissioning phase Q0 ($\sim$10 d), and Q1 ($\sim$33 d). Unfortunately, observations stopped after one month of Q17 due to a failure of the third reaction wheel. This amazing amount of Kepler data is publicly available and can be downloaded from the MAST archive[1].

Kepler data has been processed by different pipelines so far, starting with the Presearch Data Conditioning pipeline (PDC), designed to detect planetary signals. This pipeline was changed to the so-called PDC-MAP (Maximum A Posteriori) pipeline (Stumpe et al. 2012; Smith et al. 2012) because the PDC pipeline coarsely removed stellar variability signals. Recently, all Kepler data has been reprocessed by the PDC-msMAP (multiscale MAP) pipeline (Stumpe et al. 2014). This new version applies a 20-days high-pass filter intending to detect smaller planets in the data. Thus, this pipeline version is not suitable to look for stellar variability with a broad range of rotation periods since it diminishes stellar signals of slow rotators. Unfortunately, data reduced by previous pipeline versions are not publicly available anymore.

In Reinhold et al. (2013) we analyzed $\sim$40,000 active stars with a variability range $R_{\rm var} > 0.3\,\%$ (for definition see Basri et al. 2010, 2011), only using Q3 data. In $\sim$24,000 stars a clear rotation period was detected, and in $\sim$18,000 stars a second period was detected, which was assigned to surface differential rotation. Starting from this sample, we extend our analysis to all available data. Our goal is to detect consistent rotation periods throughout the quarters, and to refine previous differential rotation measurements, exploiting the much higher frequency resolution thanks to the longer time span.

[1] http://archive.stsci.edu/pub/kepler/lightcurves/tarfiles/

We do not use the much larger sample of 34,030 stars with measured rotation periods from McQuillan et al. (2014) because we are mostly interested in measuring DR. Although 20,009 stars of our sample are contained in the sample of McQuillan et al. (2014), the remaining stars either do not belong to the periodic sample of McQuillan et al. (2014), or have a smaller average variability range ($R_{\rm var} < 0.3\,\%$), rendering them unsuitable for DR measurements.

In this work we only use Q1–Q14 PDC-MAP data (version 2.1 for Q1–Q4, Q9–Q11 and version 3.0 for Q5–Q8, Q12–Q14). Q0 data was discarded because of its short time span and the much lower number of monitored targets. From Q15 on, only PDC-msMAP data was available, which is unsuitable for our purposes as explained above.

Since we are only interested in rotation-induced stellar variability, we have to exclude targets showing other kinds of periodic variability. To reduce the number of false positives, i.e., periodic variability not related to stellar rotation, we discarded 17 eclipsing binaries[2], 878 planetary candidates[3], 2 RR Lyrae stars (Kolenberg et al. 2010; Szabó et al. 2010; Benkő et al. 2010; Guggenberger et al. 2012; Nemec et al. 2011; Moskalik et al. 2012; Molnár et al. 2012; Nemec et al. 2013), and 84 γ Doradus and δ Scuti stars (Tkachenko et al. 2013; Ulusoy et al. 2014; Balona et al. 2011; Uytterhoeven et al. 2011; Lampens et al. 2013; Balona 2014). In total, 981 stars were discarded, leaving 23,143 targets, which are analyzed as described in the following section.

3. Methods

After excluding binarity stars and pulsators, we are interested in the stability of the rotational modulation. Many effects can change the shape of a light curve dominated by star spots rotating in and out of view, e.g., spots are created, others disappear while rotation takes place. The number of spots and their sizes are usually unknown. Differential rotation further hampers the detection of stable rotation periods. Sun spots change their preferred latitude of occurrence during the solar activity cycle, and therefore their rotation rate. But cyclic variability is also expected in other active stars. Moreover, Kepler suffers from instrumental effects, which are corrected by the pipeline automatically. Improper correction can mimic long-term (periodic) variability. The Kepler satellite rolls between consecutive quarters to re-orientate its solar arrays. Hence, in each quarter stars fall on different CCDs with different sensitivity.

To account for all these effects, we analyze the data of the same star in different ways. First, we apply our analysis to each quarter individually. By comparing periods of individual quarters among themselves, we shrink our initial sample to find stable rotation periods among many quarters. After that, we stitch together data from all quarters for each star in our sample, and apply a slightly different period search to the full light curve. In a last step, we analyze different segments of the full light curve, because some effects, (e.g., differential rotation) are more visible in certain segments rather than in the full time series. By comparing the periods returned by each method, we hope to detect stable rotation periods, which are unlikely caused by instrumental systematics.

[2] http://keplerebs.villanova.edu/

[3] http://archive.stsci.edu/kepler/koi/search.php

3.1. Analysis of individual quarters

To detect periodic signals in the data we use the Lomb-Scargle periodogram in a prewhitening approach as described in Reinhold et al. (2013). Each quarter is analyzed individually and in the same way. The analysis method in briefly summarized below. For details we refer the reader to the paper mentioned above.

For each star and each quarter we compute the variability range $R_{\rm var,Q}$. If $R_{\rm var,Q} > 0.3\,\%$ holds for a certain quarter, we compute five Lomb-Scargle periodograms in a successive prewhitening approach. Since computing the Lomb-Scargle periodogram is equivalent to fitting a sine wave to the data, each prewhitening step yields a set of sine fit parameters (period P_k, amplitude a_k, phase ϕ_k, and a total offset c) for $k = 1, ..., 5$. The parameters which belong to the highest peak in the periodogram yield the best parameters to fit the data. We use the returned values as initial parameters for a global sine fit to the data (t, y) according to

$$y_{fit} = \sum_{k=1}^{5} a_k \sin(\frac{2\pi}{P_k}\, t - \phi_k) + c, \tag{2}$$

This global sine wave is fit to the data through χ^2-minimization. To save computation time each light curve was binned to two hours cadences. The period associated to the highest peak in the Lomb-Scargle periodogram is called P_1, and represents the most significant period in the data.

In some cases spots are located on opposite sides of the star, and only half of the true rotation period is detected. To reduce this number of *alias* periods we compare P_1 to the set of periods P_k and their corresponding peak heights $h_k := h(P_k)$. If it holds

$$|P_1 - P_k/2| \leq 0.05\, P_1 \quad \text{and} \quad h_k > 0.5\, h_1, \tag{3}$$

then the period P_k is likely the true rotation period. In case P_1 already was the correct period, we check if there are periods P_k satisfying

$$|P_1 - 2P_k| \leq 0.05\, P_1 \quad \text{and} \quad h_k > 0.5\, h_1. \tag{4}$$

If that is not the case, the period P_k is used as rotation period, and we call this rotation period P_1.

Since our primary goal is to detect differential rotation, we look for periods adjacent to P_1. A probable second period should satisfy

$$0.01 \leq |P_1 - P_k|/P_1 \leq 0.30 \tag{5}$$

The period P_k with the second highest power in the prewhitening process satisfying Eq. 5 is called P_2. In the following section we compare period measurements of individual quarters among themselves.

3.1.1. Comparison of periods from different quarters

As discussed at the beginning of Sect. 3, the measured periods P_1 may change from quarter to quarter. That is especially true for stars exhibiting a second period P_2 because

Quarter	P_1 [d]	P_2 [d]	$R_{\rm var}$ [%]
Q01	5.51	4.98	0.69
Q02	5.71	6.06	1.41
Q03	5.39	5.14	1.55
Q04	5.47	6.04	2.34
Q05	5.34	5.74	1.78
Q06	5.48	5.12	1.63
Q07	5.44	5.20	1.86
Q08	5.30	5.81	1.78
Q09	5.38	5.79	1.44
Q10	5.33	5.74	1.32
Q11	5.37	6.02	1.79
Q12	5.29	5.89	1.66
Q13	5.37	5.95	1.66
Q14	5.64	5.26	1.17

Table 1. Period measurements of the star KIC 1163579 from Fig 1. For all quarters Q1–Q14 the star was monitored, and the variability range $R_{\rm var,Q} > 0.3\,\%$. In each quarter a second period was found, and no alias period was detected. For the star KIC 1163579 we find $\langle P_1 \rangle = 5.43\,$d.

spots may have changed their location, size, or occurrence at all. Besides that, the period P_2 might be a spurious detection in some quarters. As a first step, we look for stars with stable rotation periods throughout the quarters. To "pick and choose" the best stars shrinks our primary sample, but provides a more reliable measure of the mean stellar rotation period, and eventually the stars' DR.

For each star and each quarter $Q = 1, ..., 14$ we compute the variability range[4] $R_{\rm var,Q}$. If $R_{\rm var,Q} > 0.3\,\%$ we apply our prewhitening approach, which yields a period $P_{1,\rm Q}$. If $R_{\rm var,Q} < 0.3\,\%$, or the star was not monitored in a certain quarter, the period $P_{1,\rm Q}$ is set to zero. We only consider periods satisfying $0.5\,{\rm d} < {\rm P}_{1,\rm Q} < 45\,{\rm d}$. The upper limit accounts for the fact that we want to see at least two full rotation cycles during the limited quarter length of ~ 90 days. The lower limit should exclude pulsating stars. We compute the relative deviation of the periods $P_{1,Q}$ from their median according $|P_{1,\rm Q} - \overline{P_1}|/\overline{P_1}$. Fast rotators with a median period $\overline{P_1} < 10\,$d are allowed to differ by 10 %, stars with longer periods by 20 %. From all periods $P_{1,\rm Q}$ satisfying these criteria, we define a mean rotation period $\langle P_1 \rangle$. If more than 75 % of the periods $P_{1,\rm Q}$ satisfy this criterion, the star belongs to the so-called "good" sample. The "good" stars are shown in Fig. 6 compared to previous measurements for the whole sample. We also checked for alias periods among our set $P_{1,\rm Q}$ according to Eq. 4, but without comparing any peak heights. Periods identified as such were discarded. The star KIC 1163579, randomly chosen from our sample, is shown in Fig. 1, and its briefing is shown in Table 1. In the following section we concatenate data from individual quarters to analyze the full light curve.

3.2. Analysis of the full time series

In the previous section we only considered periods shorter than 45 days, due to the limited quarter length of ~ 90 days. Stitching together data from all available quarters is the only way to achieve two major goals: 1) the detection of periods longer than 45 days, and 2) to obtain a higher frequency resolution in the Lomb-Scargle periodogram, since the peak width scales with the inverse of the time span.

The first point is difficult to address. As mentioned earlier long-term instrumental effects are sometimes difficult to distinguish from slow rotation, especially in an automated period search of a large sample of objects. Furthermore, for this particular sample rotation periods less than 45 days were measured in Reinhold et al. (2013). Measurements of alias periods or spurious detections are possible but expected to be rare. Nevertheless, we use an upper period limit of 60 days for the analysis of the full time series.

The second point is the more interesting one because a higher frequency resolution offers the detection of individual peaks lying much closer than in the periodograms of the individual quarters. Thus, the frequency resolution is crucial for the detection of small values of differential rotation!

To achieve an almost continuous time series of each star we chose the easiest way to concatenate consecutive quarters by dividing the light curves of each quarter by its median and subtracting unity. Data outliers were removed as described in García et al. (2011). Light curves exhibiting low-frequency trends, i.e., increasing or decreasing behavior over the full 90 days window, were considered as not properly reduced by the PDC-MAP pipeline, and therefore discarded.

The method we apply to the full time series slightly differs from the previously used sine fit approach. We only compute one Lomb-Scargle periodogram of the whole time series. Due to the largely increased amount of data each light curve was binned to six hours cadences to save computation time. This sampling still enables us to detect short periods down to half a day according to the Nyquist frequency $f_{\rm Nyq} \approx 2\,{\rm d}^{-1}$. We identify the twenty highest peaks and search for periods within the limits $0.5\,{\rm d} \leq {\rm P}_1 \leq 60\,{\rm d}$. Furthermore, we force a lower peak height limit of $h_1 > 0.10$ to get some significance for P_1, and check for alias periods according to Eq. 3 and 4.

An important point to make is that we do not oversample the periodogram, in contrast to previous work (Reinhold et al. 2013). For the analysis of individual quarters oversampling was necessary because many cases only revealed a single broadened peak, rather than two or more distinct peaks. Therefore, a fine frequency sampling was necessary to subtract the correct period in the prewhitening to be able to detect more than one period. Owing to the much higher frequency resolution here, the periodogram is able to reveal individual peaks.

In the following section we try to assign a *significance* to individual peaks. The goal is to find out which peaks really carry information about different spot rotation periods, and which are related to spurious detections and/or stochastic effects, e.g., emerging and waning active regions.

3.2.1. Identification of significant peaks

Analogous to Eq. 5 we search for periods P_k within 30 % of P_1. We sort the peak heights in descending order according to $h_1 > h_2 > ...$ and compute the so-called *peak height ratio* (PHR) h_k/h_{k+1}. This method is illustrated based on the example star KIC 1163579 in Fig. 3. The idea is to detect peaks with comparable heights, and to see where the peak height drops to a significantly lower value from one peak to

[4] In the following, the variability range $R_{\rm var}$ is meant to be the median of the periods $P_{1,\rm Q}$ for the quarters Q1–Q14.

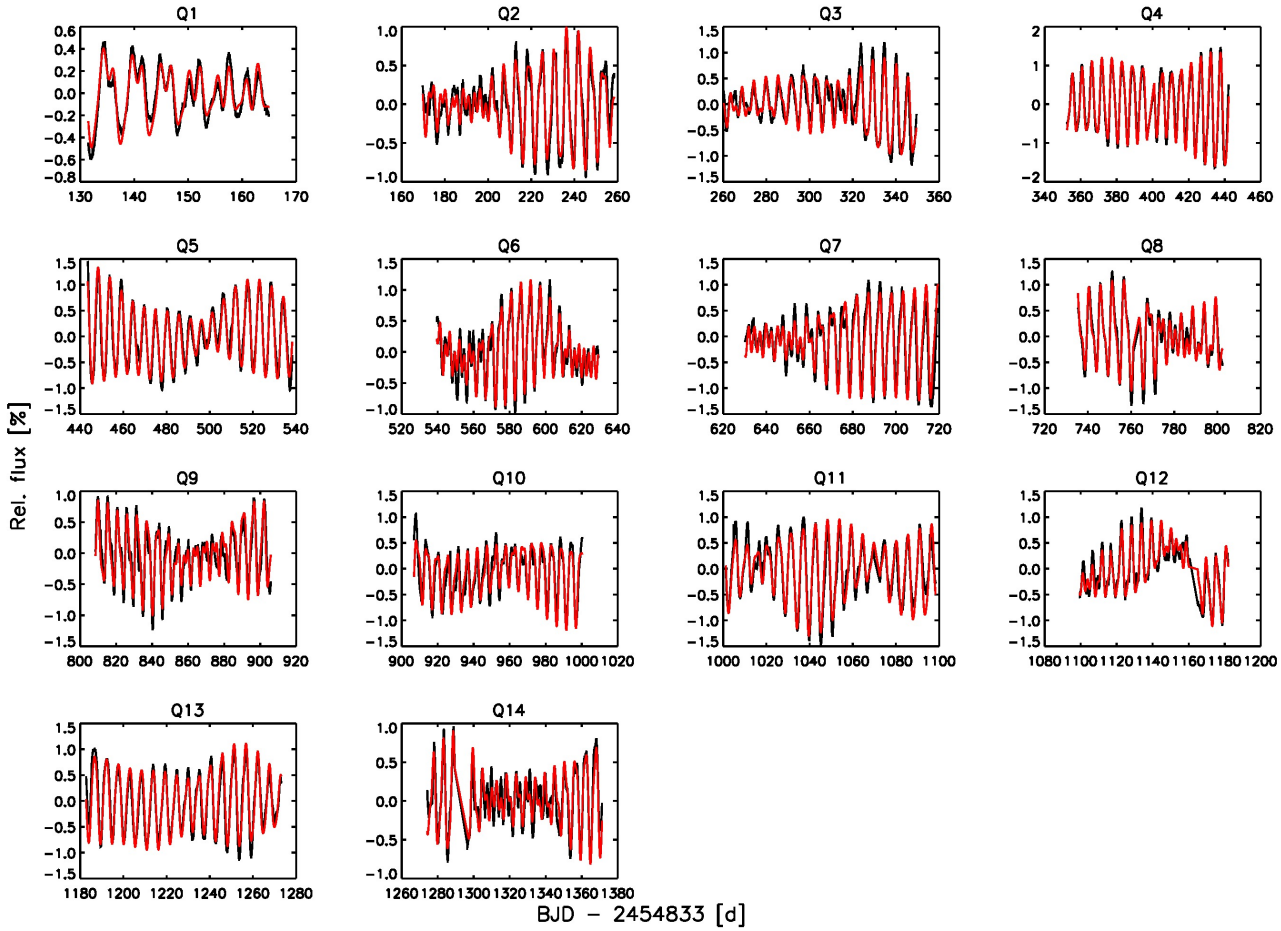

Figure 1. Light curves (black) and sine fits (red) according to Eq. 2 of the star KIC 1163579 for all quarters Q1–Q14. Period measurements of this star are given in Table 1.

the other. Hence, we compute the median of the PHR and search for the maximum deviation from this value. The related index $k = k_{\max}$ yields the number of significant peaks. In Fig. 3 the median is shown as solid red line, and the dashed red lines indicate the $\pm 1\sigma$ region. For this example, it is evident that for $k_{\max} = 3$ the PHR is at maximum, which means that the peak height of P_3 is much higher than that of P_4, compared to all peak heights within $P_1 \pm 30\,\%$. All periods P_k with $k \leq k_{\max}$ are considered as significant, the others are discarded. The lower panel of Fig. 2 shows the periodogram of the active star KIC 1163579 with the significant peaks found by this method marked in red.

3.3. Analysis of segments of the full time series

This section contains another approach we used to extract information about different periods in the data. The primary peak in the periodogram of the full time series represents the best sine fit period over the full observing time. This period must be interpreted as an average rotation period, because it fits certain parts of the light curve better than others. Adjacent peaks with less power are also needed to properly fit the data, and these periods may be more *visible* in certain segments than in the full light curve.

Minor peaks adjacent to P_1 (e.g., peaks marked by blue asterisks in the lower panel of Fig. 2) result from various phenomena: differential rotation, spot evolution, and data reduction. Differentiating between these effects is almost

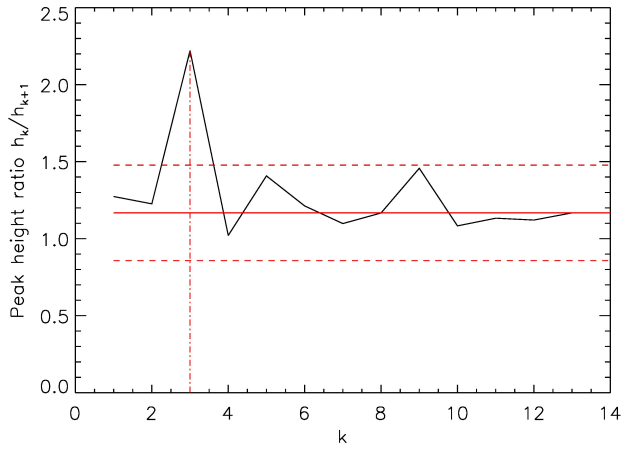

Figure 3. The peak height ratio (PHR) h_k/h_{k+1} versus peak number k of the periodogram from Fig. 2. The solid red line shows the median PHR, and the dashed red lines mark the $\pm 1\sigma$ levels. At $k = 3$ the deviation from the median is at maximum, meaning that three significant peaks were found by this method. These are marked by red asterisks in Fig. 2.

impossible, but we assume that DR is the dominating effect in most cases. Spot evolution might be the strongest

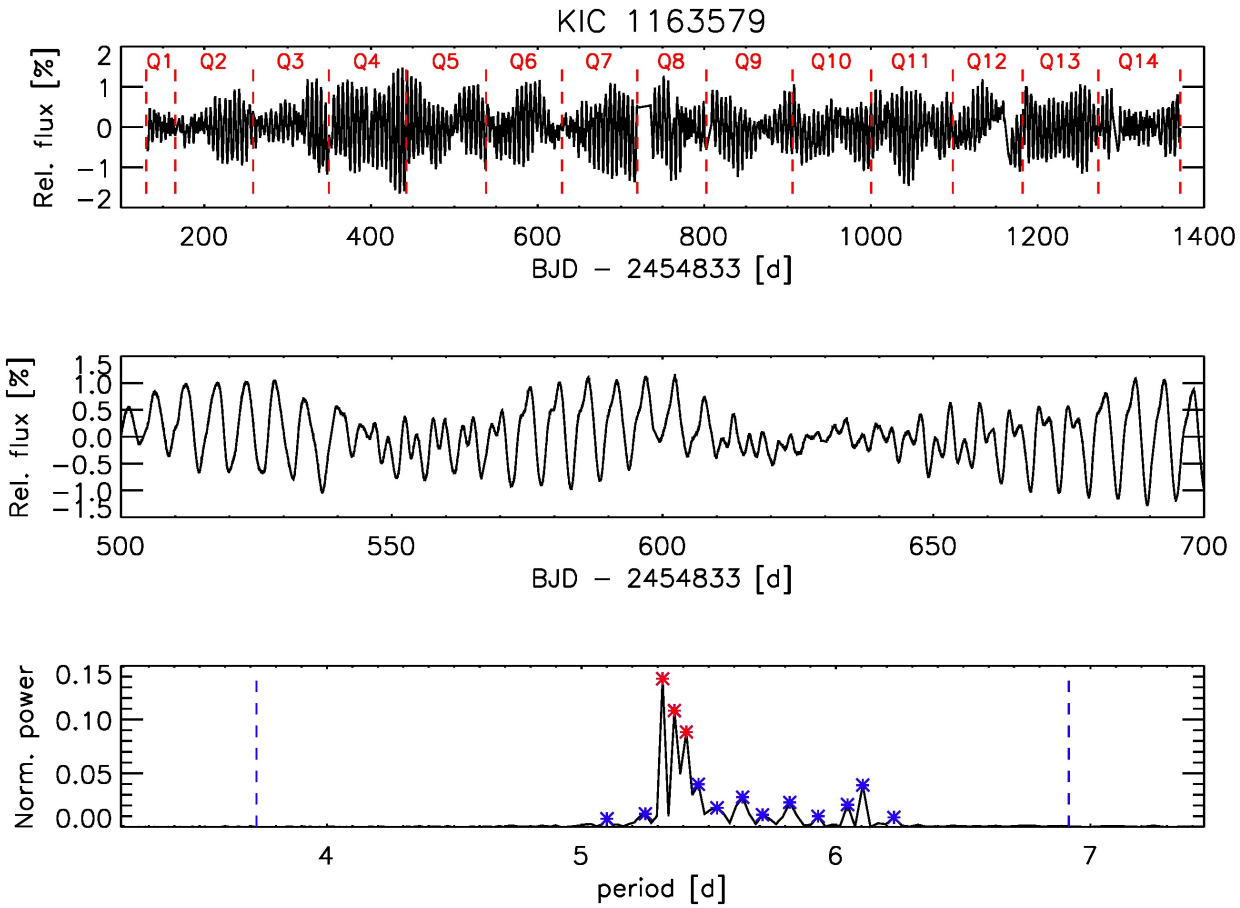

Figure 2. *Upper panel:* Full light curve of the star KIC 1163579 from quarters Q1–Q14. *Middle panel:* Zoom into the above light curve. Periodicity and the existence of a second period is clearly visible, revealed by the double-dip structure around 550 days. *Lower panel:* Periodogram of the full light curve. Significant peaks are marked in red, other peaks in the range of $P_1 \pm 30\,\%$ (indicated by the dashed blue lines) are marked in blue.

contributor of spurious detections of DR, where multiple peaks cannot be associated to spots rotating at different latitudes. Analyzing different segments thus becomes important, since the evolution of individual spots does not occur continuously in time, but may affect certain parts of the full light curve stronger than others. Another problem might be caused by stitching together individual quarters, where the end of one quarter and the beginning of the consecutive one do not agree with the overall variability pattern. This problem is intrinsic to the PDC-MAP pipeline, which was designed to remove instrumental effects from individual quarters, and not to conserve the overall variability pattern over the total observing time.

To overcome these effects we analyze segments with different lengths of the full light curve, aiming to detect periods that are stable over different time scales. In the following, segments are defined as concatenated quarters, starting with data from Q1–Q2, and adding the subsequent quarter in the next step, i.e., the second segment contains data from Q1–Q3, and so on, with the last segment being the full light curve Q1–Q14. We compute the periodogram of each segment[5], interpolate it onto the frequency grid of the periodogram of the full light curve[6], and add up the logarithmic powers of all segments. This leads to extremely clear periodograms, likely canceling spurious detections.

Fig. 4 shows periodograms of the defined segments of the star KIC 1163579, clearly revealing multiple periods between 5–6 days in all segments. The main period crystallizes out around 5.4 days. Each periodogram reveals a period around 6.1 days, which was also found in the periodogram of the full time series (s. Fig. 2), but was not considered as a significant period by our method. Thus, the measured value of DR might be largely underestimated in this case. To account for such periods with minor power, we sum up the logarithmic power of all segments, which is shown in the upper panel of Fig. 5. The main power is visible around $P_1 = 5.4$ days, and also the first and second harmonic being the half and third of this period. In certain cases it occurs that the first harmonic, $P_1/2$, has the second highest or even the highest power in the periodogram. Since we are interested in periods adjacent to P_1 we subtract a fourth order polynomial (solid blue line in Fig. 5), and exponentiate the difference, which is shown in the lower panel of Fig. 5. This procedure leads to extremely clear periodograms. Periods lying with $\pm 30\,\%$ of

[5] For the individual segments we use the normalization from Eq. 22 in Zechmeister & Kürster (2009).

[6] This is necessary because periodograms of different segments possess a different frequency resolution.

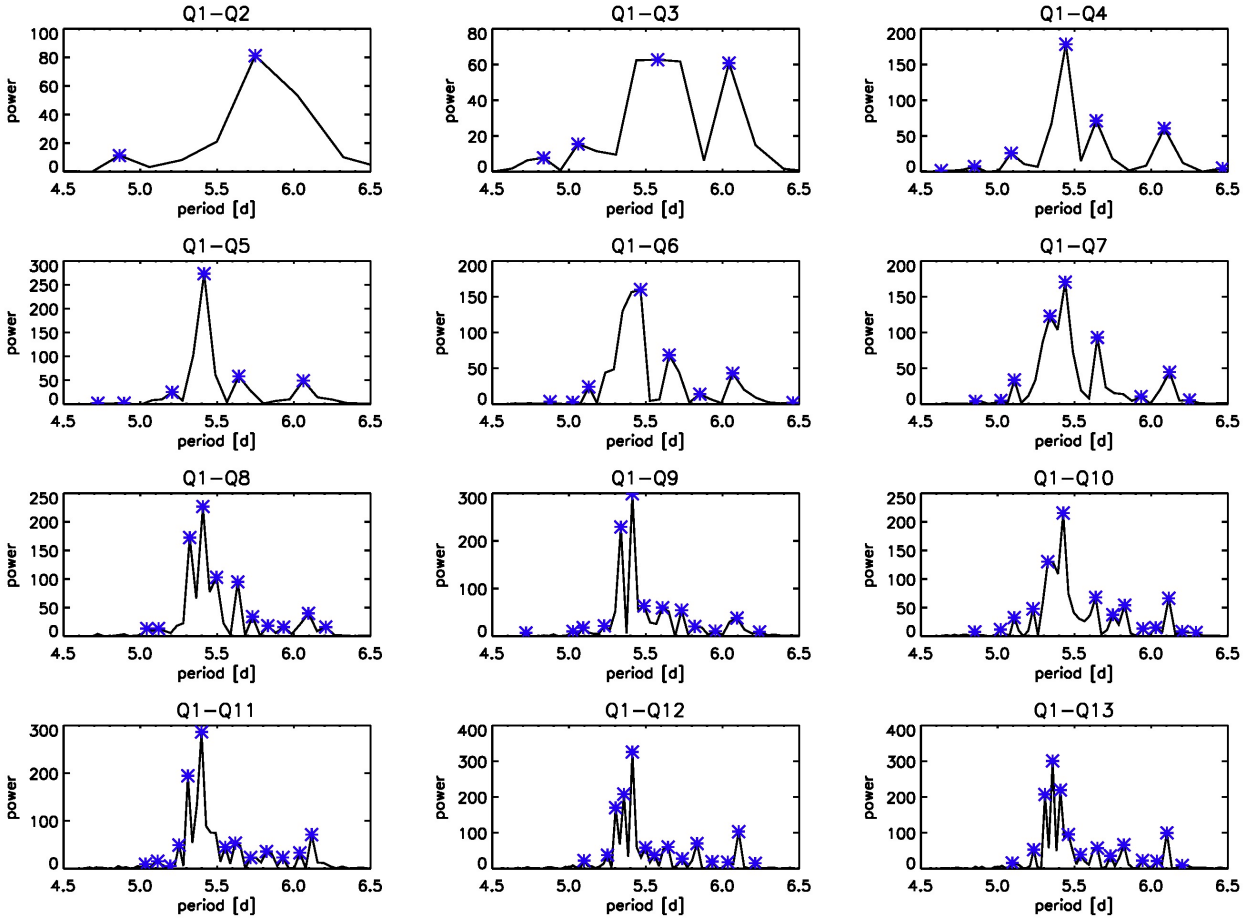

Figure 4. Periodograms of the segments of KIC 1163579. Periodicity is clearly visible between 4.5–6.5 days. The location of the main peak around 5.4 days does not change much, whereas the number of minor peaks increases toward longer segments, owing to the higher frequency resolution.

P_1 with powers $> 0.5\,h_1$ are considered as significant. The dashed red line indicates the arbitrarily chosen significance limit. The period around 6.1 days survives this procedure, and will contribute to the DR measure in Sect. 4.2. Results combining our three different approaches are presented in the following section.

4. Results

We present rotation periods of more than 18,500 stars using the different approaches from Sects. 3.1–3.3. Based on these periods we search for differential rotation in Sect. 4.2. Mean rotation periods together with their uncertainties are used to infer stellar ages through different gyrochronology relations in Sect. 4.3. Finally, Sect. 4.4 is dedicated to a small fraction of stars exhibiting rotation periods very stable in time.

4.1. Rotation periods

In Fig. 6 we present the mean rotation period $\langle P_1 \rangle$, averaged over the quarters Q1–Q14, versus color $(B-V)_0$. The black dots show previous measurements from Reinhold et al. (2013), only using Q3 data. Green dots mark the 18,691 so-called "good" stars (s. Sect. 3.1), and the 454 red and 625 blue dots indicate very stable rotators, which are discussed separately in Sect. 4.4. The dashed blue lines

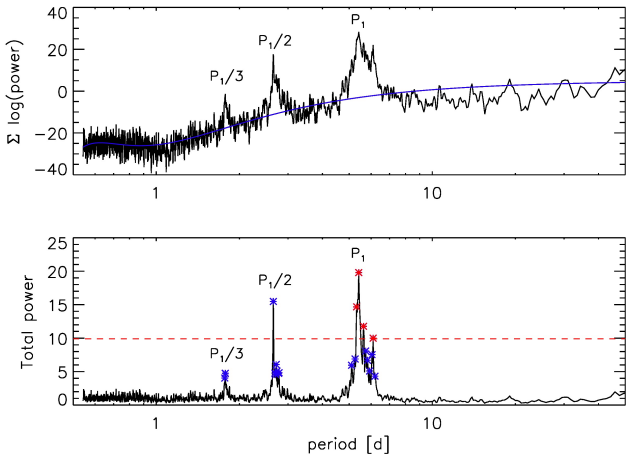

Figure 5. *Upper panel:* Summed up logarithmic powers of the periodograms of the individual segments from Fig. 4. The solid blue curve shows a fourth order polynomial fit. *Lower panel:* Exponential power of the upper panel with the polynomial fit subtracted. Peaks above the arbitrarily chosen significance limit of $0.5\,h_1$ (dashed red line) are considered as significant, and used as a measure of DR in the following. In this picture the harmonics ($P_1/2$ and $P_1/3$) are also more pronounced.

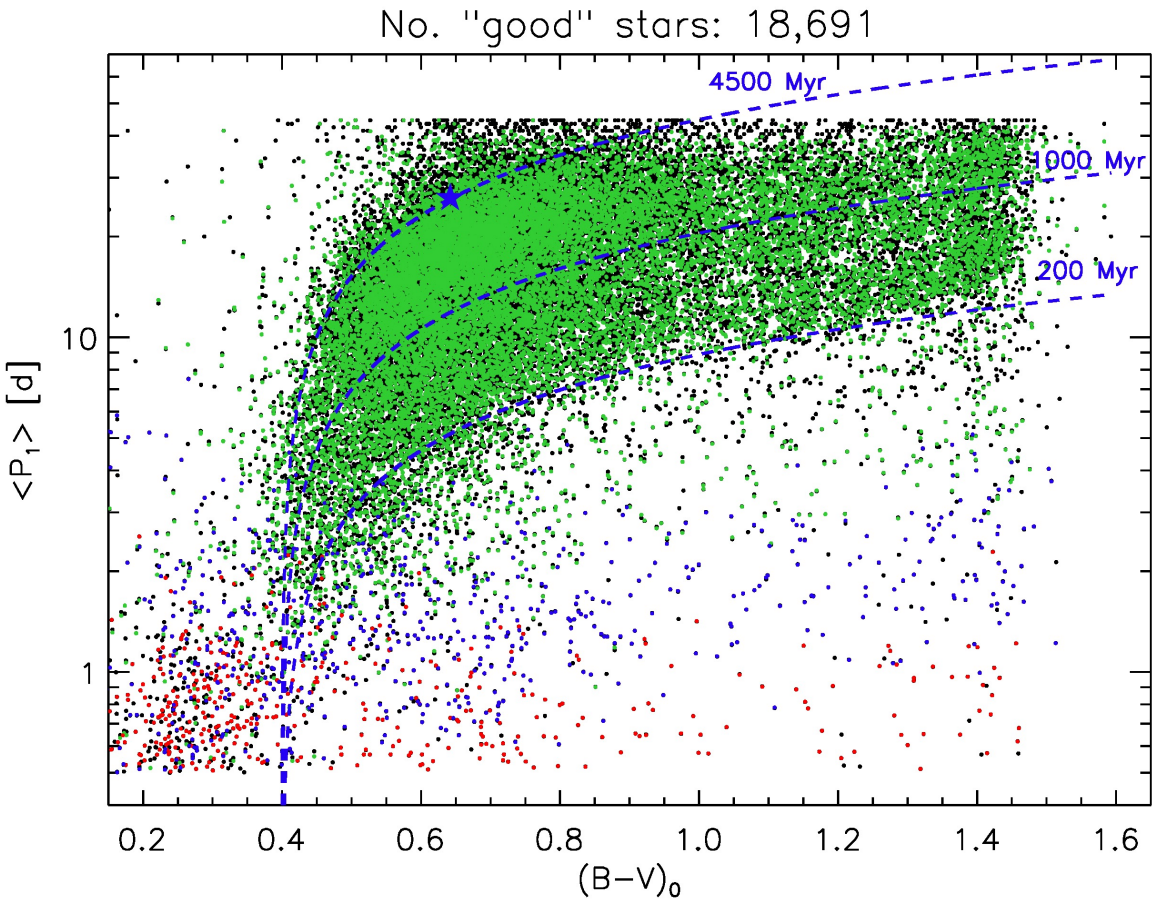

Figure 6. Mean rotation periods $\langle P_1 \rangle$ averaged over the quarters Q1–Q14 plotted against color $(B-V)_0$. Previous measurements (Reinhold et al. 2013) only using Q3 data are shown in black, "good" measurements surviving the criteria described in Sect. 3.1 are shown in green. Red and blue dots show stars with periods very stable in time, which are discussed separately in Sect. 4.4. The dashed blue lines show isochrones from Barnes (2007), and the blue star marks the position of the Sun.

show isochrones from Barnes (2007) and the blue star marks the position of the Sun. Around $(B-V)_0 = 0.4$ rotational braking due to magnetized winds becomes efficient. The 4500 Myr isochrone acts as an upper envelope to our measurements up to $(B-V)_0 \simeq 1.0$. Coeval stars redder than $(B-V)_0 = 1.0$ with supposably longer periods are missing due to the limited quarter length of $\sim$90 days. A lower envelope to the rotation period distribution is given by the 200 Myr isochrone. Stars below this curve are either younger than 200 Myr, or are not suitable for the use of gyrochronology. The latter is also true for stars bluer than $(B-V)_0 = 0.4$ (s. Sect. 4.3.1). A second group of stars immediately leaps to the eye with short periods between 0.5–2 days and $(B-V)_0 < 0.4$. Most of these stars exhibit periods very stable in time, which we discuss separately in Sect. 4.4. Comparing the black and green dots it is evident that the period measurements have been considerably improved by incorporating more data.

For the three different approaches (Sects. 3.1–3.3) we compared our measurements to the state-of-the-art rotation periods from McQuillan et al. (2014) in Fig. 7. In general, all methods show very good agreement. In each panel the dashed red line shows the one-to-one period ratio, and the upper and lower dashed blue lines indicate the 2:1 and 1:2 period ratios, respectively. The left panel shows average periods from the quarters Q1–Q14, using the green, red, and blue dots from Fig. 6. We find 17,674 stars matching the two samples. Thereof, more than 98.9 % of our measurements lie within 10 % of those from McQuillan et al. (2014). A small fraction of 0.5 % alias periods was found. The middle panel shows rotation periods derived from the analysis of the full light curve. 15,082 stars are matching, 97.4 % thereof do not differ by more than 10 %, and 1.4 % alias periods were found. The right panel shows measurements from the individual segments. 16,443 stars are matching, thereof 96.0 % within 10 %, and 2.3 % alias periods were detected.

Combined period measurements from the methods above are shown in Fig. 8. We computed the median of the periods P_1 derived from each method, allowing for a median absolute deviation (MAD) of one day for periods shorter than twenty days, and a MAD of two days for longer periods. In total, we find 18,599 stars matching with the sample of McQuillan et al. (2014). 97.6 % of the periods lie within 10 % of each other. In contrast to McQuillan et al. (2014) our sample contains stars hotter than 6500 K, and also a few stars which do not belong to their periodic sample. Since we are searching for DR in the following section, we do not restrict our sample to stars matching with McQuillan et al. (2014), but consider all stars with mea-

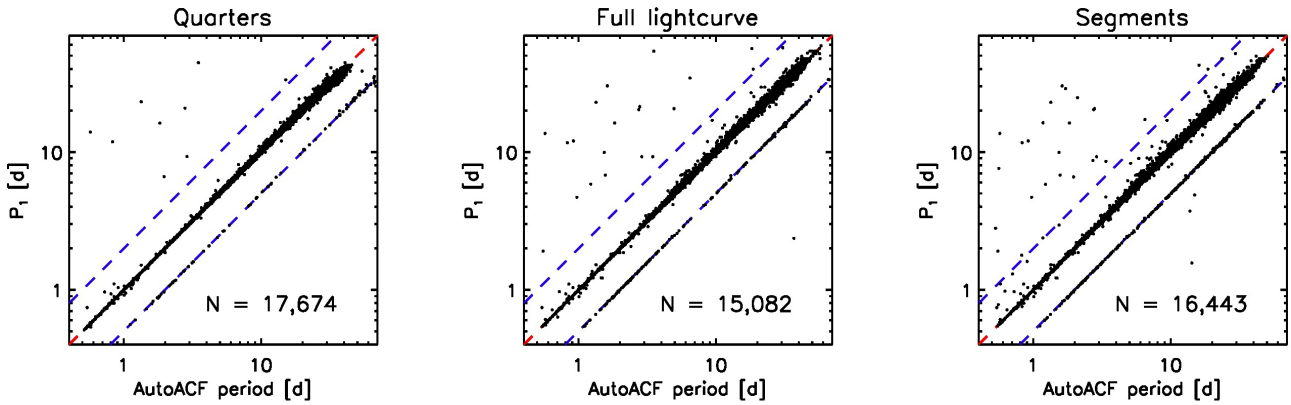

Figure 7. Comparison of rotation periods P_1 to the results of McQuillan et al. (2014) using different methods. The dashed red line denotes the 1:1 ratio, and the upper and lower dashed blue lines indicate the 2:1 and 1:2 period ratios, respectively. For each method the number of stars matching all criteria is given in the lower right corner of each panel.

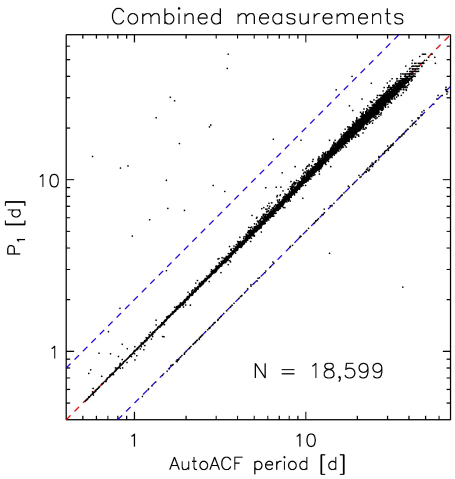

Figure 8. Rotation period measurements combining the three different approaches from Fig. 7, and comparing them to AutoACF periods from McQuillan et al. (2014).

sured period P_1 within the above MAD limits, additionally satisfying $\log g > 3.5$ and $R_{\rm var} > 0.3\,\%$.

4.2. Differential rotation

As shown in the previous section, rotation periods can be detected in a straight forward way by picking the highest periodogram peak and applying certain selection criteria. The situation is different when searching for differential rotation, acting as a perturbation to the main rotation period. We usually interpret the detection of a second period in the periodogram analysis as an indication of DR. Unfortunately, each method from Sects. 3.1–3.3 yields different results. For a certain star it occurs that one method returns a second period, whereas the other one does not. Even if all three methods yield a second period for a certain star, the periods found can differ a lot, depending on the different selection criteria and the frequency resolution. For that reason we define mean values for the DR of a certain star in the following.

We pick the minimum and maximum of the set of significant periods, individually for Sects. 3.2 and 3.3. If both methods yield a minimum and maximum period for a certain star, we compute the mean value, and call these periods $P_{\rm min}$ and $P_{\rm max}$, respectively. We refrain from calculating minimum and maximum periods from individual quarter measurements owing to their lower frequency resolution. Thus, we define the relative and absolute horizontal shear $\alpha := (P_{\rm max} - P_{\rm min})/P_{\rm max}$ and $\mathrm{d}\Omega := 2\pi\,(1/P_{\rm min} - 1/P_{\rm max})$, respectively, as a measure of DR. In the following, we show how these two quantities correlate with rotation period and effective temperature. We only consider stars exhibiting a variability range $R_{\rm var} > 0.3\,\%$, which was defined as a lower activity limit in Reinhold et al. (2013).

Fig. 9 shows the relative shear α as a function of the minimum period $P_{\rm min}$. For stars cooler than 6700 K we find that α increases with rotation period. A contrary behavior is found for hot stars ($T_{\rm eff} > 6700$ K) populating the upper left corner ($\alpha > 0.02$ and $P_{\rm min} < 2$ d). These short period stars spread a wide range of α, and clearly do not follow the overall trend. We suggest that multiple period measurements in these stars might actually be due to pulsations or rapid spot evolution, and should not be interpreted as DR. Owing to magnetic braking, cool stars exhibit longer periods, on average, thus populating the upper right part of Fig. 9. In the lower left corner ($\alpha < 0.01$ and $P_{\rm min} < 3$ d) a mixture of all temperatures is found, indicating young fast rotating stars. Again, we warn the reader that these small α values can also be mis-classified as spot evolution. The dashed blue area shows theoretical predictions from Küker & Rüdiger (2011) for models with $0.3 M_\odot$ (bottom) to $1.1 M_\odot$ (top). These simulations agree well with our observations of relative shear increasing with rotation period. Furthermore, the hot stars are not covered by the model predictions, supporting our conclusion above. Almost 78 % of the fast rotators ($P_{\rm min} < 2$ d) exhibit rotation periods very stable in time. These very stable periods are considered separately in Sect. 4.4.

We compared our findings to previous measurements from Hall (1991) who also found an increase of the relative shear with rotation period. The dash-dotted and dashed black lines show linear fits to our measurements in log-log space yielding a relation $\alpha \propto P_{\rm min}^c$ with $c = 0.71$ discarding the hot stars (blue data points) and $c = 0.55$ using all data points, respectively. The first value is consistent with the result from Hall (1991) who found $c = 0.79 \pm 0.06$.

We also compared our results to measurements from Donahue et al. (1996). These authors found a relation be-

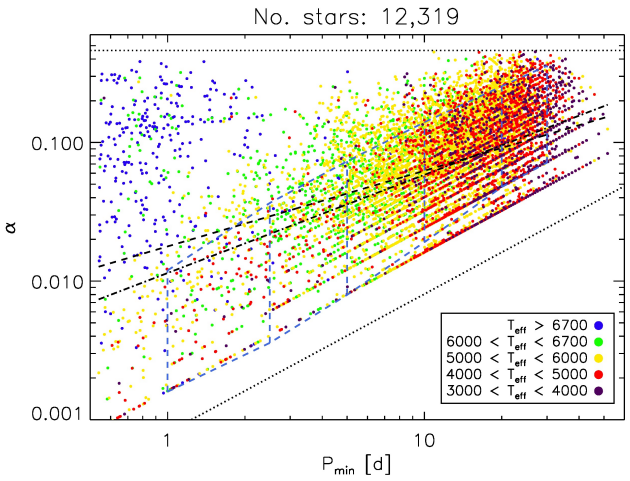

Figure 9. Minimum period $P_{\rm min}$ versus relative differential rotation α. The colors represent different temperature bins, the dotted black lines marks our detection limits. The dashed blue area shows theoretical predictions from Küker & Rüdiger (2011) for models with $0.3 M_\odot$ (bottom) to $1.1 M_\odot$ (top). We find that α increases with rotation period for stars cooler than 6700 K. The black lines show linear fits to our measurements, discarding stars hotter than 6700 K (dash-dotted line) and using all data points (dashed line), respectively.

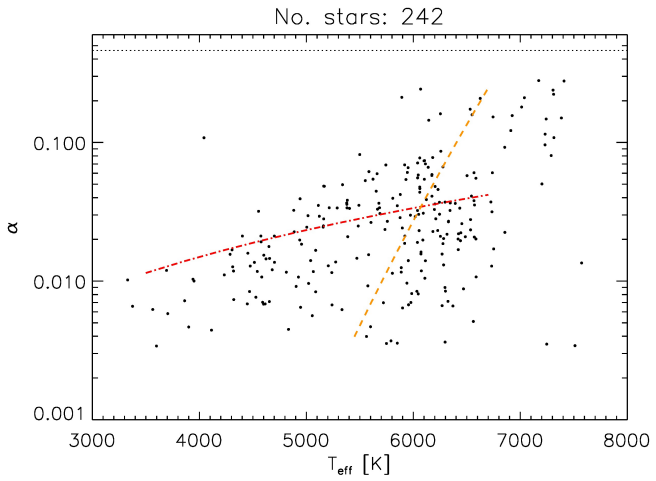

Figure 10. $T_{\rm eff}$ versus α for stars satisfying $2\,{\rm d} < {\rm P}_1 < 3\,{\rm d}$. The dash-dotted red and dashed orange curve show models from Küker & Rüdiger (2011). The dotted black line marks the upper limit of α. No distinct correlation between $T_{\rm eff}$ and α was found.

tween the mean rotation period $\langle P \rangle$ and the observed period spread ΔP according to $\Delta P \propto \langle P \rangle^{1.3\pm0.1}$. Keeping in mind that $\alpha \propto \Delta P / \langle P \rangle$, we find $\Delta P \propto \langle P \rangle^{c+1} = \langle P \rangle^{1.71}$. This value is slightly bigger than the value of 1.3 found by Donahue et al. (1996), regardless of whether discarding or keeping hot stars. The discrepancy might be explained by the fact that these authors only considered FGK stars, whereas we also incorporate M stars in our sample, usually exhibiting large values of α.

Fig. 10 shows the dependence of the relative shear on effective temperature for a subset of stars satisfying $2\,{\rm d} < {\rm P}_1 < 3\,{\rm d}$. The dash-dotted red and dashed orange curves show theoretical predictions from Küker & Rüdiger (2011) using a model with an equatorial rotation period of 2.5 days. Between 3000–6000 K the red curve matches the observations quite well, although the slope of the curve is too small. Stars hotter than 6000 K are well represented by the slope of the orange curve, although our observations are offset towards higher temperatures. We are using revised temperatures from Huber et al. (2014), being on average 200 K hotter for hot stars and 200 K cooler for cool stars, compared to previous temperatures from the KIC, which might explain this offset. We do not want to stress the comparison of our observations to the models because we do not find a clear trend when using all rotation periods. This is consistent with previous work (Reinhold et al. 2013), where only a shallow trend of α towards cooler stars has been found. We now interpret this shallow increase of α as a consequence of the increase of rotation period towards cooler stars.

In Fig. 11 we plot the absolute shear $\mathrm{d}\Omega$ against rotation period $P_{\rm min}$. We find that $\mathrm{d}\Omega$ does not strongly depend on rotation period over a wide period range. Towards fast rotators with periods on the order of a few days, the absolute shear increases, although showing large scatter. Again, we find that the upper left corner is populated by hot stars (s. Fig. 9), which are clearly separated from the overall trend. Again, we warn the reader that these large $\mathrm{d}\Omega$ values might not be associated with strong surface shear, but with different pulsation frequencies or rapid spot evolution. The dashed blue area shows theoretical models from Fig. 3 in Küker & Rüdiger (2011) with $0.3 M_\odot$ (bottom) to $1.1 M_\odot$ (top), which cover most of our measurements, but do not touch the hot stars with $\mathrm{d}\Omega > 0.1\,{\rm rad\,d^{-1}}$.

Equivalent to Fig. 9 we applied a linear fit to our measurements yielding $\mathrm{d}\Omega \propto \langle P \rangle^c \propto \langle \Omega \rangle^{-c}$ with $c = -0.29$ discarding hot stars (dash-dotted line) and $c = -0.45$ using all data points (dashed line) in Fig. 11, respectively. We find good agreement with measurements from Barnes et al. (2005) claiming $\mathrm{d}\Omega \propto \langle \Omega \rangle^{0.15\pm0.10}$, confirming the weak dependence of the absolute shear on the rotation rate.

The dependence of the absolute shear on effective temperature is shown in Fig. 12. Our measurements (gray dots) suggest the existence of two distinct regions with different behavior of $\mathrm{d}\Omega$. From 3500–6000 K the absolute shear slightly increases showing weak dependence on temperature. Above 6000 K $\mathrm{d}\Omega$ steeply increases with temperature, although showing large scatter. Data collected by Barnes et al. (2005) is plotted as purple diamonds, and the corresponding fit from Collier Cameron (2007) is shown as dotted purple line. These authors predicted a very strong temperature dependence ($\mathrm{d}\Omega \propto T_{\rm eff}^{8.9}$), which is not supported by our measurements. Light blue diamonds show measurements[7] from Ammler-von Eiff & Reiners (2012) that are in good agreement with our findings. Theoretical predictions from Küker & Rüdiger (2011) are shown as dash-dotted red and dashed orange curve. These authors found no sufficient match when fitting their results with one polynomial over the whole temperature range. Therefore, they suggested a different behavior of $\mathrm{d}\Omega$ above and below ~ 6000 K. Their curves fit remarkably well with the mean values of our measurements, shown as thick blue line. The matching gets

[7] The values were taken from Table 2 in Ammler-von Eiff & Reiners (2012) assuming an inclination of 90°.

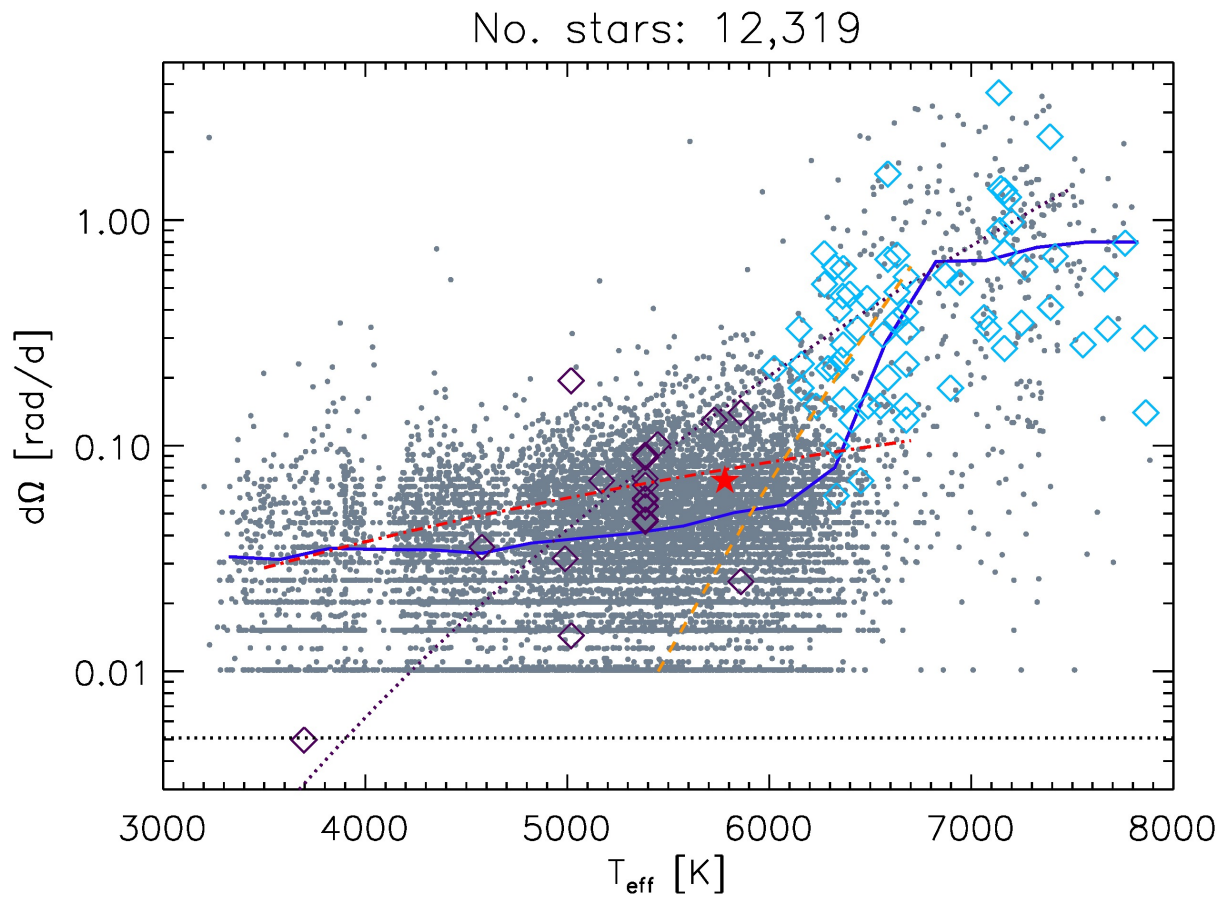

Figure 12. Effective temperature $T_{\rm eff}$ versus absolute shear $\mathrm{d}\Omega$ summarizing different measurements: Purple diamonds were taken from Barnes et al. (2005), the dotted purple curve from Collier Cameron (2007). Light blue diamonds show measurements from Ammler-von Eiff & Reiners (2012). Our measurements are shown as gray dots. The thick blue line represents the weighted mean of our measurements for 250 K temperature bins. The dash-dotted red line and the dashed orange line show theoretical predictions from Küker & Rüdiger (2011). The dotted black line represents our detection limit, and the red star marks the position of the Sun. We find that $\mathrm{d}\Omega$ shows weak dependence on effective temperature between 3300–6200 K. Above 6200 K $\mathrm{d}\Omega$ strongly increases showing large scatter.

even better when using the old KIC temperatures, rather than the new values from Huber et al. (2014), which are 200 K hotter (cooler) for the hot (cool) stars, on average. The model from Küker & Rüdiger (2011) is drawn from a star rotating with an equatorial period of $P_{\rm eq} = 2.5$ d. Our observations contain various rotation periods, which might explain the spread. In Sect. 5 we discuss reasons for the observed spread, including cases with multiple periods mis-interpreted as DR. The measured values of $P_{\rm min}$, $P_{\rm max}$, α, and $\mathrm{d}\Omega$ are collected in Table 2. The measured period differences are used as uncertainties for determining gyrochronology ages in the next section.

KIC	$T_{\rm eff}$ (K)	$R_{\rm var}$ (%)	$P_{\rm min}$ (d)	$P_{\rm max}$ (d)	α	$\mathrm{d}\Omega$ rad/d
9771948	5678	1.63	15.115	15.689	0.037	0.015
11122123	5960	1.17	9.883	10.955	0.098	0.062
2558314	4157	0.82	24.790	28.171	0.120	0.030
12317549	5793	1.06	7.377	7.996	0.077	0.066
3103637	5332	0.71	26.372	33.500	0.213	0.051

Table 2. DR measurements used in Figs. 9–12. The full table is available in machine-readable form in the online journal.

4.3. Stellar Ages

4.3.1. Gyrochronology

After measuring mean rotation periods P and period variations ΔP for two-thirds of the sample, we calculate stellar ages t along with their uncertainties Δt using different gyrochronology relations (Barnes 2007; Mamajek & Hillenbrand 2008; Meibom et al. 2009), hereafter abbreviated as B07, MH08, and MMS09, respectively. Ages are calculated according to Eq. 3 in Barnes (2007):

$$\log t = \frac{1}{n}[\log P - \log a - b \log X], \tag{6}$$

with $X := (B-V)_0 - c$ and different fit parameters a, b, c, n (see Table 3). Colors $(B-V)_0$ are obtained by converting $g-r$[8] to $(B-V)$ color using the relation from Jester et al. (2005) and subtracting the excess $B-V$ reddening $E(B-$

[8] Taken from the Kepler Input Catalog (KIC).

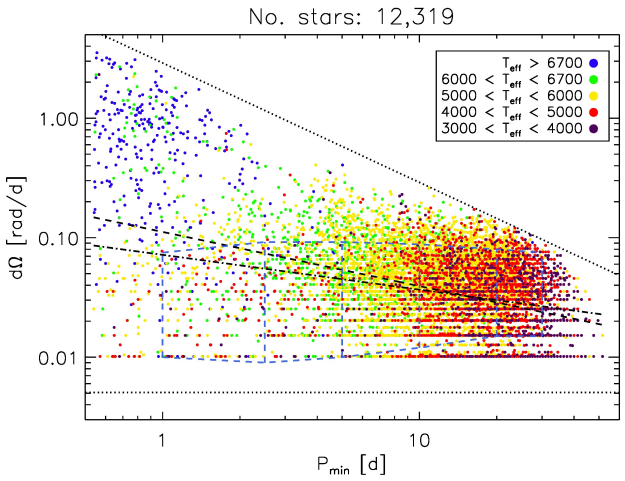

Figure 11. Minimum period $P_{\rm min}$ versus absolute differential rotation dΩ. The colors represent different temperature bins, the dotted black lines mark our detection limits. The dashed blue area shows theoretical predictions from Küker & Rüdiger (2011). We found that dΩ is almost independent of rotation period over a wide period range, but slightly increases towards short periods. Stars hotter than 6700 K do not follow the overall trend. The black lines show linear fits to our measurements, discarding stars hotter than 6700 K (dash-dotted line) and using all data points (dashed line), respectively.

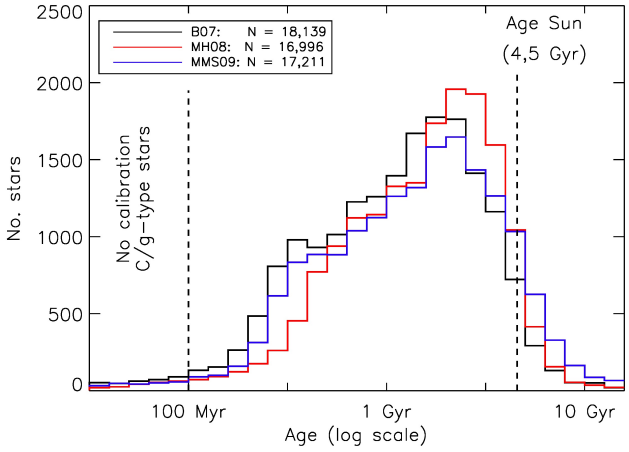

Figure 13. Stellar age distributions derived from different gyrochronology relations: Barnes (2007); Mamajek & Hillenbrand (2008); Meibom et al. (2009). Their calibration ranges are given in Table 3. Stars with derived ages younger than 100 Myr (left of the dashed black line) should be treated with caution.

Ref.	a	b	c	n	$(B-V)_0$	P [d]
B07	0.7725	0.601	0.400	0.5189	≥ 0.42	≥ 1.5
MH08	0.4070	0.325	0.495	0.5660	≥ 0.51	≥ 1.5
MMS09	0.7700	0.553	0.472	0.5200	≥ 0.50	≥ 1.5

Table 3. Fit parameters and period and color constraints used in the different gyrochronology relations.

V)[8]. Age uncertainties are calculated according to Eq. 10 in Barnes (2007):

$$\Delta t = \frac{t}{n}\sqrt{(\Delta P/P)^2 + (b\,\Delta X/X)^2 + d\theta^2}, \qquad (7)$$

with $\Delta P := (P_{\rm max} - P_{\rm min})/2$ being the uncertainty of the mean period P, and ΔX being the $(B-V)$ difference between the conversion from Jester et al. (2005) and Bilir et al. (2005). Frequently, this difference is rather small, and no uncertainties for the SDSS $g-r$ colors were found in the literature. Thus, we set a minimum uncertainty of ± 0.01 mag to the $(B-V)$ colors with smaller uncertainties. The term $d\theta^2$ contains uncertainties of the fit parameters from Table 3 (compare Eq. 10 in Barnes 2007). If DR was detected the period uncertainty dominates the age uncertainty, especially for the slowly rotating stars with ΔP on the order of a few days.

Distributions of the derived ages are shown in Fig. 13. For our stellar ages sample we retain stars that are not contained in the McQuillan et al. (2014) sample, but remove those with stable rotation periods (s. Sect. 4.4). The latter might not have spun down to the I-sequence yet (s. Barnes 2003 for terminology), or their rotation might be controlled by non-eclipsing companions. Additionally, we tighten our limit of the surface gravity to $\log g \geq 4.2$ to ensure that gyrochronology relations are only applied to dwarf stars.

The MH08 and MMS09 distributions contain less stars than the B07 distribution owing to the different color ranges (see Table 3). The color and period constraints are needed to ensure that our field star sample obeys the same (or at least a similar) dependence of rotation period on color and age as the cluster stars used for calibration. The derived ages are collected in Table 4, and their reliability is discussed in more detail in Sect. 5.

Derived ages younger than 100 Myr should be treated with caution. These stars cover the full $(B-V)_0$ range, but mostly exhibit rotation periods less than five days. They likely have not yet converged to the I-sequence, and thus are not suitable for applying gyrochronology relations. The right edge of the distribution with derived ages older than 10 Gyr can also not be trusted since roughly half of the stars exhibit ages older than the universe. These values result from a combination of long rotation periods ($P > 20$) days and effective temperatures > 5500 K, with either or both of them being erroneous.

Using the B07 distribution 17,623 stars possess ages between 100 Myr and 10 Gyr. Thereof, 90.7 % are younger than 4 Gyr, in good agreement with Matt et al. (2015) estimating ~ 95 % comparing the sample from McQuillan et al. (2014) to model predictions. Less than 0.62 % of the derived ages are greater than 10 Gyr, and less than 2.2 % of the B07 stars lie in the critical calibration region younger than 100 Myr, providing some confidence in the derived age distribution.

4.3.2. Activity-age relation

Inspired by Fig. 8 in Soderblom et al. (1991) we are interested in deriving a similar activity-age relation. Unfortunately, spectra of Kepler stars are lacking, so we cannot compare the derived ages to the established chromospheric activity measure $R'_{\rm HK}$. Nevertheless, the variability range $R_{\rm var}$ can be used as an activity indicator in a statistical sense. Using the B07 distribution we plot the age against the variability range in Fig. 14, which was inspired

KIC	$R_{\rm var}$ (%)	$T_{\rm eff}$ (K)	$(B-V)_0$ (mag)	$\Delta(B-V)_0$ (mag)	P (d)	ΔP (d)	$t_{\rm B07}$ (Myr)	$\Delta t_{\rm B07}$ (Myr)	$t_{\rm MH08}$ (Myr)	$\Delta t_{\rm MH08}$ (Myr)	$t_{\rm M09}$ (Myr)	$\Delta t_{\rm M09}$ (Myr)	flag
7799260	2.14	5437	0.671	0.010	23.837	0.000	-	-	-	-	-	-	ev
11135449	1.20	4731	1.032	0.010	31.783	0.775	2197	162	3154	364	2370	313	-
3751292	4.21	6089	0.556	0.010	3.656	0.000	172	16	241	35	279	48	-
8481446	0.39	5699	0.628	0.010	15.115	0.000	1710	134	1892	222	2213	259	-
3757951	6.17	5345	0.677	0.010	1.918	0.006	-	-	-	-	-	-	vs

Table 4. Rotation periods, $(B-V)_0$ colors, and gyrochronology ages using different calibrations. If no ages are provided, either the period or the color lies outside the valid calibration range (see Table 3). *Super-stable* and *very stable* stars (flagged as "ss" and "vs", respectively) were discarded from the stellar ages sample. Furthermore, stars with $\log g < 4.2$ may have *evolved* off the main sequence (flagged as "ev"). For these stars we provide a rotation period but no ages since gyrochronology relations are not calibrated for evolved stars. Further table entries are the KIC number, the variability range $R_{\rm var}$, and the effective temperature $T_{\rm eff}$.

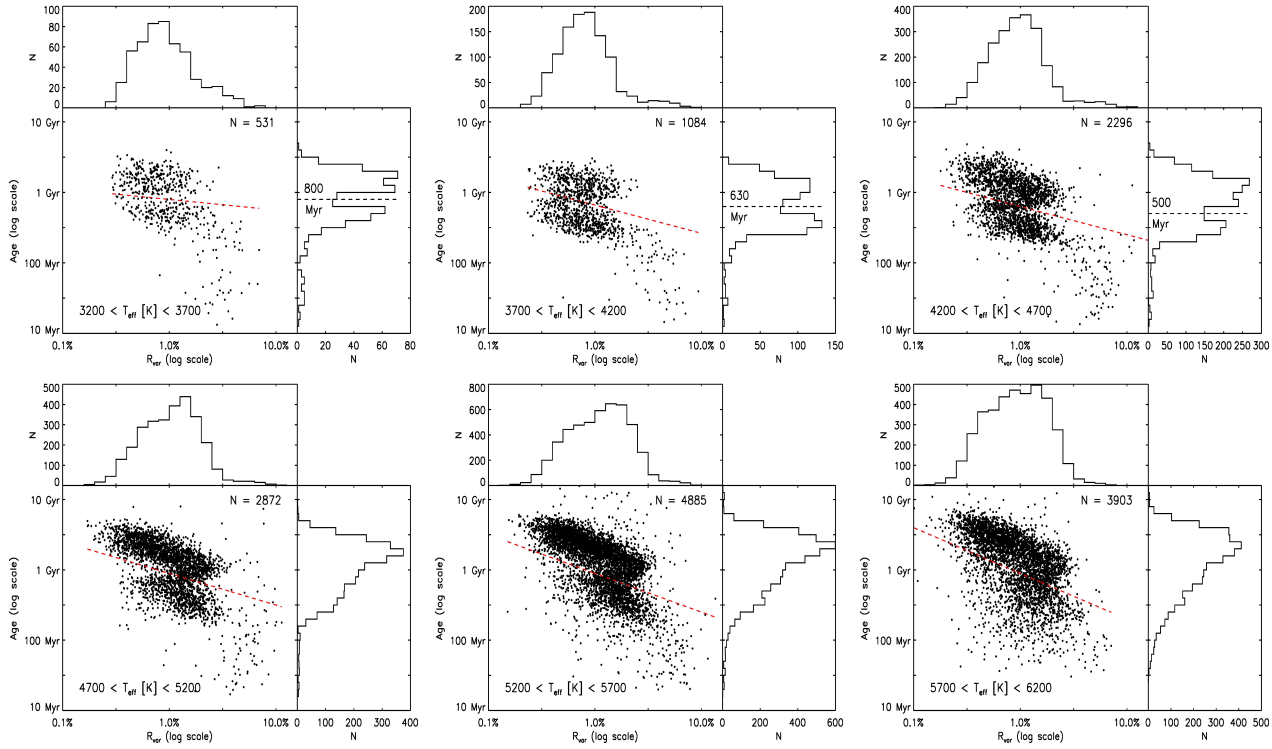

Figure 14. Gyrochronology ages plotted against the variability range for 500 K temperature bins between 3200–6200 K. The age distribution shows a bimodality between 3200–4700 K, which vanishes for hotter stars. The variability range $R_{\rm var}$ decreases with age, becoming more emphasized towards hotter stars (increasing slope of dashed red line).

by Fig. 4 in McQuillan et al. (2014). The ages were derived only using periods lying closer than 10 % to periods found by McQuillan et al. (2014). From the upper left to the lower right, the temperature increases from 3200–6200 K in 500 K intervals. The upper panels (3200–4700 K) shows a bimodality of the age distribution, which vanishes for hotter stars. This incident was first detected by McQuillan et al. (2013a) for the Kepler M dwarf periods, and confirmed later that the bimodality extends to hotter stars (Reinhold et al. 2013; McQuillan et al. 2014). Moreover, the gap separating the two peaks shifts towards younger stars with increasing temperature, starting at $\sim$800 Myr for the coolest stars (3200–3700 K), and descends to 500 Myr for stars between 4200–4700 K. For each temperature bin the point distribution shows that the variability range decreases with age, although each distribution exhibits large scatter in $R_{\rm var}$. This general behavior is expected from the observation that young stars are, on average, more active than old ones. In each panel two point clouds are visible. Thus, we separated the two clouds into a so-called *young* and *old* sample. To guide the eye we empirically drew a dashed red line between the two samples, with increasing slope towards hotter temperatures, and varying offset in each panel. Stars lying below (above) the dashed red line belong to the *young* (*old*) sample, respectively. There are other ways of defining a *young* and an *old* sample, e.g., using the horizontal dashed black line separating the two peaks of the bimodal distribution, but we wanted to emphasize the correlation between activity and age. We were curious if the parameters of these distinct samples substantially differ. Thus, we plotted histograms of common stellar parameters such as $\log g$, FeH, brightness, and so on. Unfortunately, we found no major difference in the parameters that could explain the evidence of the two point clouds. However, we found a correlation between the ages shown and the corresponding peak heights of the primary periodogram peaks. The peak

heights of the *young* sample were, on average, higher than the peaks of the *old* sample. We interpret this result in terms of young stars being more active. Hence, their light curves are more sinusoidal, because they suffer less by DR, spot evolution, or instrumental flaws, all effects disrupting the light curve shape.

4.4. Extremely stable periods

From the analysis of the individual quarters we found periods $P_{1,\mathrm{Q}}$ that are extremely stable in time. These stars have previously been shown in Fig. 6, and are analyzed in more detail here. To quantify their temporal stability we computed the median absolute deviation $\mathrm{MAD}(\mathrm{P}_1) := \overline{|\mathrm{P}_{1,\mathrm{Q}} - \langle \mathrm{P}_1 \rangle|}$, and categorized two groups of stable periodic stars: *super-stable* stars with $\mathrm{MAD}(\mathrm{P}_1) < 0.001$ d, and *very stable* stars satisfying $0.001 < \mathrm{MAD}(\mathrm{P}_1) < 0.01$ d. These stars are flagged in the last column of Table 4. We emphasize that these periods are stable over more than three years of observation!

Figure 15 shows the periods and effective temperatures of both groups. *Super-stable* and *very stable* periods are shown as red and blue dots, respectively. Inner green dots denote stars where a second period was found. The temperature and period distributions are shown in the upper and right panel, respectively. The period distribution shows that most of the *super-stable* stars exhibit short periods less than one day, with a mean period of $\langle P_1 \rangle = 0.95$ d. The *very stable* stars extend to longer periods up to ~ 12 d, with a mean of $\langle P_1 \rangle = 1.90$ d. Stars with a second period were found in both groups, but only between 0.5–4.2 days. The temperature distribution shows that the vast majority of both groups exhibit temperatures less than 8000 K, with a mean of ~ 6800 K for the *super-stable* stars. The *very stable* stars are, on average, 700 K cooler. Both distributions populate the full temperature range, but stars with a second period were almost exclusively found below 8000 K. Between 8000–10,000 K a dearth of second period stars was found, and only few second period stars were found above 10,000 K.

There exist two general explanations for the observed stable periodic variability. One possible explanation are stellar pulsations, which are known to be very stable in time. The other process serving as an astronomical clock is synchronization by a companion. We calculated the $\mathrm{MAD}(\mathrm{P}_1)$ with the intention of disentangling these two processes. In the period regime of 0.5–4 days δ Scuti, γ Dor, and hybrid pulsators thereof are expected. The boundaries of the so-called *instability strip* (i.e., the region in the Hertzsprung–Russell diagram populated by these pulsators) is expected roughly between 6500–8800 K. Surprisingly, most of the stable stars exhibit temperatures less than 8000 K. A fraction of them might actually be γ Dor stars between 6500–7000 K, but there is no pulsation mechanism able to produce such stable periods in the cool stars regime. Stable periods above 8000 K are likely caused by pulsations because spots are not necessarily expected for such hot stars. Thus, we favor the conclusion that the periodicity of stars cooler than 6500 K is caused by spots on the stellar surface stabilized by non-eclipsing companions, either due to interactions with another star or a close-in planet. Moreover, this hypothesis is supported by the observation that stars with multiple periods (indicative for DR) were mostly found below 8000 K.

5. Discussion

5.1. Rotation

- We measured rotation periods for a statistically meaningful ensemble of stars. In total, more than 18,500 rotation periods we derived using different approaches, all revealing very good agreement with the results from McQuillan et al. (2014).
- As discussed in the previous section, we found 1079 periods extremely stable in time, with a median absolute deviation less than 0.01 d. For stars cooler than 6500 K binarity is the favored explanation. In our total sample (see Table 4) we have 5124 stars with $P_1 < 10$ d and $T_{\mathrm{eff}} < 6500$ K. 573 of these stars exhibit stable periods, which corresponds to a percentage of ~ 11.2 %. van Saders & Pinsonneault (2013) state that tidally synchronized binaries are fast rotators with periods less than 10 days and that they contaminate the field with 4 %, compared to 11 % in the Hyades (Duquennoy & Mayor 1991). Our rate is almost three times higher than the expected percentage of tidally locked field star binaries, but comparable to the expected percentage in the Hyades. One possible explanation may be the existence of non-transiting planets, which are able to decrease the angular momentum loss rate due to magnetized winds (Cohen et al. 2010). Additionally, pulsating stars cooler than 6500 K might contribute to this rate. Other explanations for stable rotation might be different dynamos. Brown (2014) suggests the so-called *Metastable Dynamo*, where stars are born rapidly rotating with weak coupling to the wind. Other dynamo mechanisms might generate strong magnetic fields leading to long spot lifetimes.

5.2. Differential rotation

- Exact values of α and $\mathrm{d}\Omega$ are hard to determine, and depend on the particular threshold used. Depending on which periods are selected as P_{min} and P_{max}, the absolute values of α and $\mathrm{d}\Omega$ can differ a lot. Nevertheless, each method from Sects. 3.1–3.3 produces the same correlations for α and $\mathrm{d}\Omega$ with temperature and period. Combined measurements from the different approaches, as described at the beginning of Sect. 4.2, were used to provide average values of P_{min} and P_{max}. As discussed by the example of Fig. 12 the observed spread in $\mathrm{d}\Omega$ can only partially be explained by theory. Collier Cameron & Donati (2002) and Donati et al. (2003) found a large spread in $\mathrm{d}\Omega$ ranging from $0.046 - 0.091\,\mathrm{rad\,d^{-1}}$ for the active star AB Dor. Evolving spot configurations might be an explanation. Hence, all measurements here should be interpreted in a statistical way.
- Although the derived values are method dependent, the statistical averages are not. Our results are in good agreement with previous measurements (Hall 1991; Donahue et al. 1996) and theoretical predictions (Küker & Rüdiger 2011).
- Simulations of spotted stars exhibiting rapid spot evolution are able to generate beat-shaped light curves, multiple periodogram peaks, and therefore able to mimic

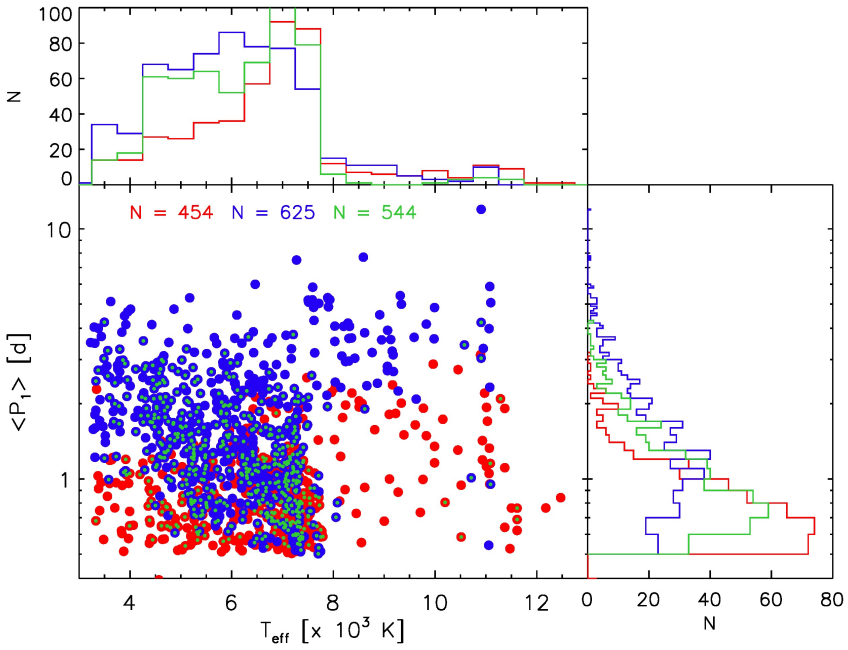

Figure 15. Stars with *super-stable* periods ($\mathrm{MAD}(P_1) < 0.001$ d, red), and *very stable* periods ($0.001 < \mathrm{MAD}(P_1) < 0.01$ d, blue). The inner green dots denote stars where a second period was found. The temperature and period distributions are shown in the top and right panel, respectively.

DR. This interpretation was not considered so far. We think that spot evolution may play a role, but we have no way to discriminate between these two phenomena.

5.3. Stellar Ages

- All gyrochronology relations have been calibrated by ground-based observations of open clusters and Mount Wilson stars. The stars used in the different calibrations exhibit different period and color ranges. Age calibration was performed using the Sun as an age anchor. Thus, the relations are not tested for stars older than the Sun. Applying these relations to stars with a wider period and color range might lead to less accurate ages. mean which
- Gyrochronology ages are most reliable between 500–2500 Myr. Depending on their braking efficiency some stars younger than 500 Myr may not have converged to the I-sequence yet. Thus, their periods may not be suitable for the use of gyrochronology. The calibration becomes even worse for stars with derived ages less than 100 Myr. Such stars might belong to the C-sequence, obeying a physically different behavior. We do not trust derived ages younger than 100 Myr or older than 10 Gyr.
- Subgiants and main sequence stars obey a different rotation-age relationship (García et al. 2014). In this study we attempt to exclude evolved stars by setting a lower limit to the surface gravity of $\log g \geq 4.2$. Unfortunately, Kepler does not provide stellar luminosity classification, so our sample might be contaminated by subgiants. Contamination might be as large as 35 % for field stars as pointed out by van Saders & Pinsonneault (2013).
- The existence of the two point clouds in Fig. 14 for stars with $3200 < T_{\mathrm{eff}} < 4700$ K is a matter of debate. McQuillan et al. (2014) suggested that the bimodality of the age distribution can be understood in terms of two distinct star formation events in the solar neighborhood. Stellar ages are correlated with the variability range in the sense that young stars are more active, on average. Interestingly, this trend becomes more distinct towards hotter stars, as indicated by the dashed red line in Fig. 14, which lacks an explanation so far.
- A comparison of gyrochronology and asteroseismology ages is challenging. Much progress was recently made (see, e.g., Angus et al. 2015). Most rotation period and asteroseismology samples do not overlap because strong activity, essential for achieving spot rotation periods, damps mode excitation (Chaplin et al. 2011). Furthermore, Kepler lacks bright stars, which are needed for asteroseismology. Upcoming missions will hopefully change this unpleasant situation in the near future.

6. Summary

We re-analyzed the sample of 24,124 stars from Reinhold et al. (2013) using Q1–Q14 data. Good agreement was found with previous rotation periods and measurements from McQuillan et al. (2014). We searched for deviations from the mean rotation period using the Lomb-Scargle periodogram in different approaches, aiming to detect multiple significant periods, and assigning them to surface differential rotation. The general trends of the DR with period and temperature, observed in Reinhold et al. (2013), could all be confirmed although individual measurements of α and $\mathrm{d}\Omega$ may differ due to the different frequency resolution of the full time series and the 90-days time base of a single quarter. In general, the new measurements are in very good agreement with previous observations (Hall 1991; Donahue et al. 1996) and theoretical predictions (Küker & Rüdiger 2011). Stellar ages were derived from gyrochronology relations provided by different authors, with uncertainties that are dominated by the period spread. A bimodal age distribution was found between 3200–4700 K, vanishing for hotter star. The derived ages show a correlation with the variability range serving as an activity indicator. Furthermore, we found 1079 stars exhibiting a very stable period, with a median absolute deviation less than 0.01 d.

The almost constant periods of the hot stars may be explained by pulsations, whereas the stability of the cooler star ($T_{\rm eff} < 6500\,{\rm K}$) may be explained with synchronization of the orbital period of a non-eclipsing companion.

Acknowledgements. We would like to thank the referee for providing very constructive suggestions, which led to significant improvements to the paper, especially to the differential rotation discussion. We acknowledge support from Deutsche Forschungsgemeinschaft Collaborative Research Center SFB-963 "Astrophysical Flow Instabilities and Turbulence" (Project A18).

References

Affer, L., Micela, G., Favata, F., & Flaccomio, E. 2012, MNRAS, 424, 11
Ammler-von Eiff, M. & Reiners, A. 2012, A&A, 542, A116
Angus, R., Aigrain, S., Foreman-Mackey, D., & McQuillan, A. 2015, MNRAS, 450, 1787
Balona, L. A. 2014, MNRAS, 437, 1476
Balona, L. A., Cunha, M. S., Kurtz, D. W., et al. 2011, MNRAS, 410, 517
Barnes, J. R., Collier Cameron, A., Donati, J.-F., et al. 2005, MNRAS, 357, L1
Barnes, S. A. 2003, ApJ, 586, 464
Barnes, S. A. 2007, ApJ, 669, 1167
Barnes, S. A. 2010, ApJ, 722, 222
Basri, G., Walkowicz, L. M., Batalha, N., et al. 2011, AJ, 141, 20
Basri, G., Walkowicz, L. M., Batalha, N., et al. 2010, ApJ, 713, L155
Benkő, J. M., Kolenberg, K., Szabó, R., et al. 2010, MNRAS, 409, 1585
Bilir, S., Karaali, S., & Tunçel, S. 2005, Astronomische Nachrichten, 326, 321
Brown, T. M. 2014, ApJ, 789, 101
Chanamé, J. & Ramírez, I. 2012, ApJ, 746, 102
Chaplin, W. J., Basu, S., Huber, D., et al. 2014, ApJS, 210, 1
Chaplin, W. J., Bedding, T. R., Bonanno, A., et al. 2011, ApJ, 732, L5
Cohen, O., Drake, J. J., Kashyap, V. L., Sokolov, I. V., & Gombosi, T. I. 2010, ApJ, 723, L64
Collier Cameron, A. 2007, Astronomische Nachrichten, 328, 1030
Collier Cameron, A., Davidson, V. A., Hebb, L., et al. 2009, MNRAS, 400, 451
Collier Cameron, A. & Donati, J.-F. 2002, MNRAS, 329, L23
Delorme, P., Collier Cameron, A., Hebb, L., et al. 2011, MNRAS, 413, 2218
do Nascimento, Jr., J.-D., García, R. A., Mathur, S., et al. 2014, ApJ, 790, L23
Donahue, R. A., Saar, S. H., & Baliunas, S. L. 1996, ApJ, 466, 384
Donati, J.-F., Collier Cameron, A., & Petit, P. 2003, MNRAS, 345, 1187
Doğan, G., Metcalfe, T. S., Deheuvels, S., et al. 2013, ApJ, 763, 49
Duquennoy, A. & Mayor, M. 1991, A&A, 248, 485
García, R. A., Ceillier, T., Salabert, D., et al. 2014, A&A, 572, A34
García, R. A., Hekker, S., Stello, D., et al. 2011, MNRAS, 414, L6
Guggenberger, E., Kolenberg, K., Nemec, J. M., et al. 2012, MNRAS, 424, 649
Hall, D. S. 1991, in Lecture Notes in Physics, Berlin Springer Verlag, Vol. 380, IAU Colloq. 130: The Sun and Cool Stars. Activity, Magnetism, Dynamos, ed. I. Tuominen, D. Moss, & G. Rüdiger, 353
Huber, D., Silva Aguirre, V., Matthews, J. M., et al. 2014, ApJS, 211, 2
James, D. J., Barnes, S. A., Meibom, S., et al. 2010, A&A, 515, A100
Jester, S., Schneider, D. P., Richards, G. T., et al. 2005, AJ, 130, 873
Kolenberg, K., Szabó, R., Kurtz, D. W., et al. 2010, ApJ, 713, L198
Küker, M. & Rüdiger, G. 2011, Astronomische Nachrichten, 332, 933
Lampens, P., Tkachenko, A., Lehmann, H., et al. 2013, A&A, 549, A104
Lebreton, Y. & Goupil, M. J. 2014, A&A, 569, A21
Mamajek, E. E. & Hillenbrand, L. A. 2008, ApJ, 687, 1264
Matt, S. P., Brun, A. S., Baraffe, I., Bouvier, J., & Chabrier, G. 2015, ApJ, 799, L23
McQuillan, A., Aigrain, S., & Mazeh, T. 2013a, MNRAS, 432, 1203
McQuillan, A., Mazeh, T., & Aigrain, S. 2013b, ApJ, 775, L11
McQuillan, A., Mazeh, T., & Aigrain, S. 2014, ApJS, 211, 24
Meibom, S., Barnes, S. A., Latham, D. W., et al. 2011a, ApJ, 733, L9
Meibom, S., Barnes, S. A., Platais, I., et al. 2015, Nature, 517, 589
Meibom, S., Mathieu, R. D., & Stassun, K. G. 2009, ApJ, 695, 679
Meibom, S., Mathieu, R. D., Stassun, K. G., Liebesny, P., & Saar, S. H. 2011b, ApJ, 733, 115
Molnár, L., Kolláth, Z., Szabó, R., et al. 2012, ApJ, 757, L13
Moskalik, P., Smolec, R., Kolenberg, K., et al. 2012, arXiv:1208.4251
Nemec, J. M., Cohen, J. G., Ripepi, V., et al. 2013, ApJ, 773, 181
Nemec, J. M., Smolec, R., Benkő, J. M., et al. 2011, MNRAS, 417, 1022
Nielsen, M. B., Gizon, L., Schunker, H., & Karoff, C. 2013, A&A, 557, L10
Noyes, R. W., Hartmann, L. W., Baliunas, S. L., Duncan, D. K., & Vaughan, A. H. 1984, ApJ, 279, 763
Pallavicini, R., Golub, L., Rosner, R., et al. 1981, ApJ, 248, 279
Perryman, M. A. C., Brown, A. G. A., Lebreton, Y., et al. 1998, A&A, 331, 81
Pizzolato, N., Maggio, A., Micela, G., Sciortino, S., & Ventura, P. 2003, A&A, 397, 147
Reinhold, T., Reiners, A., & Basri, G. 2013, A&A, 560, A4
Skumanich, A. 1972, ApJ, 171, 565
Smith, J. C., Stumpe, M. C., Van Cleve, J. E., et al. 2012, PASP, 124, 1000
Soderblom, D. R. 2010, ARA&A, 48, 581
Soderblom, D. R., Duncan, D. K., & Johnson, D. R. H. 1991, ApJ, 375, 722
Stumpe, M. C., Smith, J. C., Catanzarite, J. H., et al. 2014, PASP, 126, 100
Stumpe, M. C., Smith, J. C., Van Cleve, J. E., et al. 2012, PASP, 124, 985
Szabó, R., Kolláth, Z., Molnár, L., et al. 2010, MNRAS, 409, 1244
Tkachenko, A., Aerts, C., Yakushechkin, A., et al. 2013, A&A, 556, A52
Ulusoy, C., Stateva, I., Iliev, I. K., & Ulaş, B. 2014, arXiv:1401.1964
Uytterhoeven, K., Moya, A., Grigahcène, A., et al. 2011, A&A, 534, A125
van Saders, J. L. & Pinsonneault, M. H. 2013, ApJ, 776, 67
Vidotto, A. A., Gregory, S. G., Jardine, M., et al. 2014, MNRAS, 441, 2361
Walkowicz, L. M. & Basri, G. S. 2013, MNRAS, 436, 1883
Zechmeister, M. & Kürster, M. 2009, A&A, 496, 577